Volume 7 | Number 9 | 7 March 2019 | Pages 4193–5044

Journal of Materials Chemistry A

Materials for energy and sustainability

rsc.li/materials-a

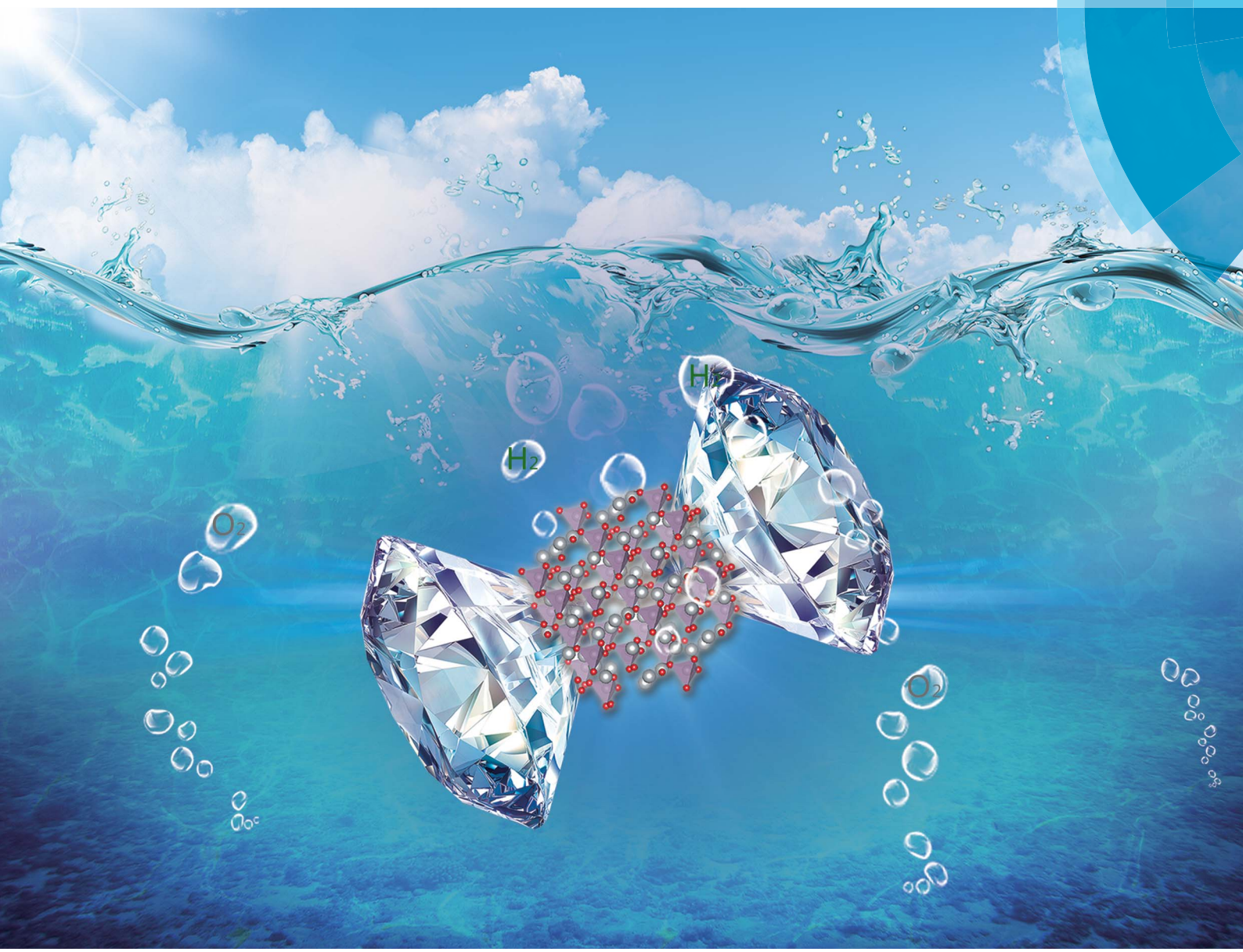

ISSN 2050-7488

ROYAL SOCIETY OF CHEMISTRY | Celebrating IYPT 2019

PAPER

Hao Yan *et al.*

Pressure-driven band gap engineering in ion-conducting semiconductor silver orthophosphate

Journal of Materials Chemistry A

PAPER

Check for updates

Cite this: J. Mater. Chem. A, 2019, 7, 4451

HPSTAR 690-2019

Pressure-driven band gap engineering in ion-conducting semiconductor silver orthophosphate†

Yang Lu, ‡[a] Shengcai Zhu,‡[ab] Eugene Huang,[a] Yu He, [ac] Jiaji Ruan,[a] Gang Liu[a] and Hao Yan *[a]

Received 4th November 2018
Accepted 31st December 2018

DOI: 10.1039/c8ta10606a

rsc.li/materials-a

The obtainment of active semiconductor photocatalysts remains a challenge for converting sunlight into clean fuels. A pressing need is to explore a novel method to tune the electronic band structures and gain insightful knowledge of the structure–property relationships. In this work, taking silver orthophosphate (Ag_3PO_4) as an example, a static pressure technique is applied to modulate the band gap and indirect–direct band character *via* altering its crystal structure and lattice parameters. Under ambient conditions, cubic Ag_3PO_4 possesses an indirect-band gap of ~2.4 eV. At elevated pressure, the band gap of Ag_3PO_4 narrowed from 2.4 eV to 1.8 eV, reaching the optimal value for efficient solar water splitting. During the pressure-induced structural evolution from cubic to trigonal phases, the indirect-to-direct band gap crossover was predicted by first-principles calculations combined with structure search and synchrotron X-ray diffraction experiments. Strikingly, the observed band gap narrowing was partially retained after releasing pressure to ambient pressure. This work paves an alternative pathway to engineer the electronic structure of semiconductor photocatalysts and design better photo-functional materials.

Introduction

Ion-conducting semiconductors are a versatile class of materials with attractive applications including energy conversion and storage due to their outstanding properties in mechanics, optics, and electrical transport.[1–6] Typically, silver ion conductors usually possess an optical band gap (E_g), such as the fast-ionic conductor α-AgI (E_g~ 2.8 eV) and a newfound ductile semiconductor α-Ag_2S (E_g ~ 0.9 eV).[2,6] Recently, the ion-conducting Ag_3PO_4 (E_g ~ 2.4 eV) was used as a novel photocatalyst for water splitting and waste-water cleaning.[1] Its visible-light-response, photo-oxidation activity and extremely high quantum yield of ~90% at wavelengths less than ~480 nm have aroused wide interest in exploiting the silver-based photocatalysts.[1,7–14] However, the relatively wider band gap and indirect-band gap nature of Ag_3PO_4 under ambient conditions lead to narrower solar spectrum absorption and lower optical absorption coefficients, which in turn limit its photocatalytic efficiency.

For a single semiconductor photocatalyst, a direct-band gap of 1.5–2.2 eV is optimal for meeting the requirements of solar-driven water splitting, which can theoretically reach the maximum solar-to-hydrogen conversion efficiency of more than 12.4% under air mass 1.5 global (AM1.5G) solar illumination.[15–18] Numerous attempts have been made to modulate the electronic band structure and improve the photocatalytic performance of Ag_3PO_4 by ion doping, crystal-facet engineering, and homo/hetero-junction construction.[9,13,19–25] These methods, however, suffer from the difficulty of incorporating suitable ions into the Ag_3PO_4 lattice with superior photocatalytic activity, which is partially due to the high-energy barrier of inserting an arbitrary dopant into a strong [PO_4] matrix; or they lead to slight changes in the surface electronic structure rather than the bulk. It is therefore highly desirable to explore an alternative strategy to engineer the electronic band structure further while also retaining the band gap.

According to theoretical calculations, yellow Ag_3PO_4 can be treated as black Ag_2O (E_g ~ 1.2 eV) with incorporated p-block species, where the phosphorus atoms contribute negligibly to the total density of states, *i.e.*, the configuration and size of [AgO_x] polyhedra dominate the band structure of Ag_3PO_4.[1,14] Herein, taking Ag_3PO_4 as an exploratory platform, the static pressure technique, an effective and clean approach to alter the crystal structure and precisely modulate the lattice parameters as well as the electronic wave functions,[26,27] was applied to tune

[a]Center for High Pressure Science & Technology Advanced Research, Shanghai 201203, China. E-mail: yanhao@hpstar.ac.cn

[b]Department of Physics and Astronomy, High Pressure Science and Engineering Center, University of Nevada, Las Vegas, NV 89154, USA

[c]Key Laboratory of High-Temperature and High-Pressure Study of the Earth's Interior, Institute of Geochemistry, Chinese Academy of Sciences, Guiyang, Guizhou 550081, China

† Electronic supplementary information (ESI) available: Morphology (SEM), elemental analysis (EDX), and malleability of the sample, pressure-dependent optical properties (Tauc plot), Raman spectra, synchrotron XRD spectra of pristine and quenched samples, typical Rietveld refinement results of the high-pressure phase, simulated XRD spectra, calculated volume–pressure plot and energy–volume plot, partial charge density of VBM and CBM bands, and density of states (DOS). See DOI: 10.1039/c8ta10606a

‡ These authors contributed equally to this work.

the electronic band structure of the photocatalyst and unveiled a correlation with the configuration of the [AgO_x] matrix. Strikingly, the band gap of Ag_3PO_4 under compression narrowed from 2.37 eV to 1.82 eV, achieving the optimal band gap for efficient solar water splitting. Using density functional theory (DFT) calculations, the indirect-to-direct band gap crossover was discovered during the pressure-induced structural evolution from the cubic to trigonal phases. Interestingly, the shrinking band gap was partially retainable after releasing pressure to ambient conditions mainly due to the slight distortion of the [AgO_x] polyhedra. These results could provide a guideline for engineering the band structure of materials and designing highly active photocatalysts.

Experimental

Diamond anvil cell sample loading

The silver orthophosphate powder (Ag_3PO_4, Alfa Aesar, 99%) was loaded into a Mao–Bell type symmetric diamond anvil cell (DAC, 300 μm culets) with a ruby chip for pressure determinations. T301 stainless steel or rhenium foil (250 μm in thickness) was pre-indented to 40 μm in thickness and a hole was laser drilled ($\lambda = 1064$ nm, power < 0.3 W) at the indentation center to serve as the gasket and sample chamber. Silicone oil was employed as the pressure-transmitting medium (PTM). The pressures were measured with the *in situ* ruby fluorescence technique.[28] The accuracy of pressure determination is better than 2 GPa at the highest pressure of this study, considering the generation of non-hydrostatic conditions by silicone oil upon pressure beyond 6 GPa.[29]

In situ high-pressure structural characterization

The *in situ* high-pressure angle-dispersive X-ray diffraction (AD-XRD) experiments were executed in the Shanghai Synchrotron Radiation Facility (SSRF, BL15U1), Advanced Light Source (ALS, BL12.2.2), and Stanford Synchrotron Radiation Lightsource (SSRL, BL10-2) with wavelengths of 0.6199, 0.49594, and 0.6199 Å. The resulting two-dimensional patterns were integrated using Fit2D software.[30] Rietveld refinements were performed using the General Structure Analysis System (GSAS) with the user interface EXPGUI package.[31,32] The *in situ* high-pressure Raman spectroscopy experiments were performed on a Raman spectroscopy system in the backscattering configuration with an excitation laser ($\lambda = 532$ nm, Renishaw 1000). The spectral resolution is better than 1.02 cm^{-1}.

In situ high-pressure optical measurements

The powdered Ag_3PO_4 sample was pressurized (up to 3 GPa) using a DAC without a PTM to form a film with a thickness of ~10 μm for accurate optical absorption studies.[33] Then, two pieces of polycrystalline platelets were peeled off the diamond culet and together with a ruby chip were loaded into the DAC sample chamber, using silicone oil as the PTM. The high-pressure UV-vis spectroscopy measurements were carried out using a micro UV-vis spectroscopy system (DH-2000-BAL, Ocean Optics). During compression and decompression, the Ag_3PO_4 sample color change was photographed using an optical microscope (Leica M205C).

Global structure search

The potential energy surface (PES) of Ag_3PO_4 was explored using a DFT based Stochastic Surface Walking (SSW) global structure search (SSW-DFT). The SSW method[34,35] is an unbiased, automated approach to explore the multidimensional PES of complex systems by taking into account the second derivative information. The efficiency of the method for exploring the PES has been demonstrated for both aperiodic (molecules and clusters) and periodic (surfaces and crystals) systems. The algorithm of the SSW global optimization method can be found in the literature. In detail, the potential energy surface of Ag_3PO_4 was determined in a 16-atom (2 Ag_3PO_4 units per cell) Ag_3PO_4 lattice, using the cubic structures of Ag_3PO_4 as seeds, which is the most stable phase under ambient conditions. In the SSW search, we generally performed a series of parallel runs (4–10 depending on the system) starting from the initial guess structures, and up to 300 minima were collected at the first stage, from which the most stable configuration was obtained. Next, we verified the result with the experiment results. If the most stable configuration of the first stage was inconsistent with the experiment, then another 300 minima were collected. This process was repeated until the configuration is consistent with the experiment. *Via* the random search, we found the most stable configuration, which agreed well with the experiment (see the following section).

Stochastic Surface Walking (SSW) pathway sampling

The SSW algorithm has an automated climbing mechanism to drive an atomic configuration from a local energy-minimum state to a high-energy configuration along random directions, inheriting the idea of the bias-potential driven constrained-Broyden-dimer (BP-CBD) method for the transition-state (TS) location.[36] Three steps are involved for finding the lowest energy pathway, as described below briefly. (i) Pathway collection. In SSW pathway sampling, firstly, we start from one single phase (starting phase) and utilize the SSW method to explore all the likely phases near the phase. A structure selection module is utilized to decide whether to accept/refuse once a new minimum is reached. If the new phase that is different from the starting phase is identified by the SSW crystal method,[37] we record/output the IS (*i.e.* starting phase) and the FS (a new phase) of the current SSW step. Then, the program will return to the IS by rejecting the new minimum to continue the phase exploration; on the other hand, if the new minimum identified by SSW is still the starting phase (*e.g.*, the same symmetry but a permutation isomer with a varied lattice), the program will accept the new isomeric phase and start the phase exploration from this phase. We repeated this procedure until a certain number of IS/FS pairs were obtained. (ii) Pathway screening. Secondly, we utilized the variable-cell double-ended surface walking (DESW) method[38] to establish a pseudopathway connecting the IS to the FS for all IS/FS pairs. The approximate barrier is obtained according to the DESW pseudopathway, where the maximum energy point along the pathway is generally a good estimate for the true TS.[38] By sorting the approximate barrier

 This journal is © The Royal Society of Chemistry 2019

height, we can obtain the candidates for the lowest energy pathways. (iii) Lowest energy pathway determination. Thirdly, the candidates for the lowest energy pathways are selected to exactly locate the true TS by using the DESW TS-search method.[38] By sorting the exact barrier calculated, the energy difference between the TS and the IS, and the lowest energy pathways could be finally obtained. All the lowest energy pathways will be further confirmed by extrapolating the TS towards the IS and FS, and the TSs need to be validated by phonon spectrum calculations, showing one and only one imaginary mode. In this study, we explore the structural transformation between the cubic Ag_3PO_4 phase and the high-pressure Ag_3PO_4 phases, using the SSW method. Based on the sampled free energy landscape, the pathways connecting the initial structure and the final structure on the potential energy surface can be determined in an atom-to-atom correspondence, and we further export the pathway by the nudged elastic band (NEB) method.[39]

DFT calculation details

All calculations were performed using the plane-wave DFT program, Vienna Ab initio Simulation Package (VASP)[40] where the electron-ion interaction of Ag, P, and O atoms is represented by the projector augmented wave (PAW) scheme and the exchange–correlation functional assumes the GGA-PBE. In the SSW pathway sampling, 16-atom Ag_3PO_4 supercells at 10 GPa were used. In order to speed up the PES exploration, we adopted the following parameter settings: a kinetic energy plane-wave cutoff of 400 eV and a Monkhorst–Pack k-point mesh of $(4 \times 4 \times 4)$ for 16-atom supercells. Once the low-energy pathways were located, we switched to high-accuracy calculations using a plane-wave cutoff of 800 eV and a denser Monkhorst–Pack k-point mesh $(8 \times 8 \times 8)$ for 16-atom supercells. For all the structures, both the lattice and atomic positions were fully optimized until the maximum stress component was below 0.1 GPa and the maximum force component was below 0.01 eV $Å^{-1}$. It is well known that GGA severely underestimates band gaps; thus we calculated the density of states using the PBE0 hybrid exchange–correlation functional.

Results

High-purity Ag_3PO_4 powder (Fig. S1†) was employed to study the electronic structural change and atomic structural evolution through pressure treatments (Fig. 1a). Upon pressurizing, the

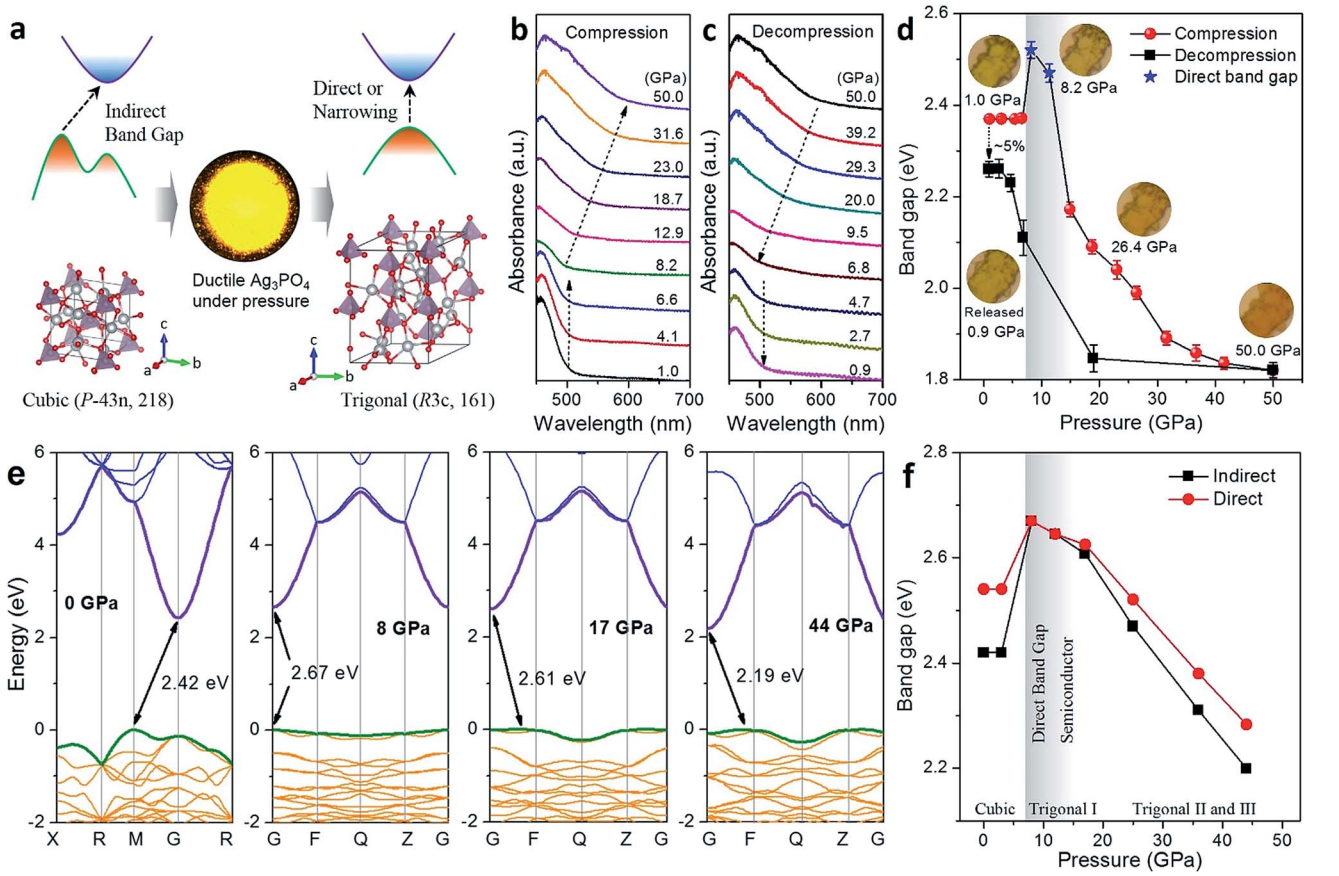

Fig. 1 (a) Scheme of the electronic band structure and crystal structure transitions for the Ag_3PO_4 semiconductor by pressure treatment. (b and c) UV-vis absorption spectra of Ag_3PO_4 under compression and decompression, respectively. (d) Optical band gap as a function of pressure derived from the absorption spectra. The indirect band gap is denoted by red (spherical) and black (square) data points, and the direct band gap is denoted by the blue (star) data points. (e) Calculated band structures for Ag_3PO_4 with a cubic phase (0 GPa) and trigonal phases of I (8 GPa), II (17 GPa), and III (44 GPa). (f) The theoretical direct/indirect band gap of Ag_3PO_4 as a function of pressure.

yellow powder could be easily made into a sheet between the diamond culets, showing excellent malleability (Fig. S2†). Then, the pressure effects on the optical properties of this sheet-formed material were explored by *in situ* UV-vis absorption spectroscopy. Fig. 1b and c show the absorption spectra of the typical Ag_3PO_4 slice under compression and decompression, respectively. As pressure increased from ambient to 50 GPa, the position of the absorption edge shows a red shift from 500 nm to around 650 nm, accompanying a change in the slope of the absorption edge (Fig. S3†). The band gap of Ag_3PO_4 as a function of pressure (Fig. 1d) was derived from the absorption spectra *via* the Tauc method (Fig. S4†).[41] Below the critical pressure of 7.5 GPa, the indirect band gap was 2.37 eV, agreeing with a previous report and remained stiff, which corresponds to the cubic phase.[1] The region with the direct band gap is marked with a gray background between 7.5 GPa and 15 GPa, where the direct band gap of Ag_3PO_4 with a trigonal-I phase jumped up to ~2.5 eV and then decreased with a further increase in pressure. After the direct-to-indirect transition, the indirect band gap of the sample monotonically narrowed to 1.82 eV with increasing pressure, achieving the optimal value of the band gap for solar water splitting. Meanwhile, the color of the sample changed from yellow to orange during compression, as evidenced in the inserted photographs of the Ag_3PO_4 slice (Fig. 1d). Upon decompression, the band gap hysteretically broadened from 1.82 eV to 2.26 eV, while the color changed back to yellow. A more thrilling fact is that the band gap of the quenched sample under ambient conditions decreased by 5% compared with the starting material, which may lead to an enhancement of photocatalytic activity.

The electronic band structures of Ag_3PO_4 with different phases were calculated using the DFT method with the PBE0 hybrid exchange–correlation functional, overcoming the severely underestimated band gap of the exchange–correlation functionals, such as LDA and GGA. As shown in Fig. 1e, the energy band configurations of the cubic and trigonal phases are very different, implying their distinction in optical properties. In detail, the band gap at ambient pressure is 2.42 eV, which is very consistent with the 2.37 eV from experiment. Interestingly, the indirect-to-direct band gap crossover occurred after the phase transition from the cubic to the trigonal-I phase. As pressure increased to more than 17 GPa, the indirect band gap reappeared in the trigonal-II and III phases. Fig. 1f summarizes the pressure-dependent indirect and direct band gap of Ag_3PO_4. Obviously, the energy difference between the direct and indirect band gap for Ag_3PO_4 decreased from ~120 meV to 0 eV when the cubic phase shifted to trigonal-I. Subsequently, the difference gradually increased to ~80 eV at 44 GPa for the trigonal-III phase.

The structural evolution should dominate the variations of the electronic structure, then the indirect/direct bandgap transitions and bandgap tuning under pressure. In this work, Raman spectroscopy and angle-dispersive synchrotron X-ray diffraction (AD-XRD) experiments associated with theoretical calculations were conducted under pressure to gain the local and global structural information. Under ambient conditions, Ag_3PO_4 possesses a body-centered cubic structure ($P\bar{4}3n$, no. 218) with a lattice parameter of ~6.01 Å.[42–44] In this structure, the regular [PO_4] tetrahedra, constituting the body-centered cubic lattice, are isolated by highly distorted [AgO_4] tetrahedra and each oxygen atom coordinates with one phosphorus atom and three silver atoms. Owing to the greater electronegativity of P relative to the Ag atom, the P–O bonds are stronger than the covalent-like Ag–O bonds. This then results in a prominent Raman peak at a frequency of 908 cm^{-1} for ambient Raman spectra (Fig. S5a and S5b†), which could be identified as the symmetry stretching vibration of the [PO_4] tetrahedron.[45–48] Based on the group theory analysis, the cubic structure of Ag_3PO_4 has 10 Raman-active modes with mechanical representation $\Gamma = A_1 + 3E + 6T_2$. To date, these Raman modes were not fully measured for Ag_3PO_4 under ambient conditions, which is partially due to the weak vibration intensity or the overlapping of modes. In high-pressure Raman experiments, the Raman mode with the strongest vibration trended to a higher frequency with increasing pressure, except the turning range near 7.5 GPa with a red shift of 2 cm^{-1} (Fig. S5a, b, d and e†), which indicated the phase transition of Ag_3PO_4. Meanwhile, the prominent Raman peaks gradually broadened after a sharp jump around the phase transition point (Fig. S5c and S5f†), suggesting the slight distortion of the lattice under elevated pressure. During decompression to ambient pressure, the broadened Raman peaks could not be fully recovered, while the frequency of the [PO_4] phonon mode rapidly reverted to the original position except the hysteresis during the high-pressure phase.

Knowledge of pressure-induced structural evolution can be gained from synchrotron X-ray diffraction (XRD) spectra. Fig. 2a shows the XRD patterns of Ag_3PO_4 under compression up to 50 GPa and decompression to ambient pressure. All the Bragg peaks shifted towards higher angles when pressure was applied up to 5.2 GPa due to unit cell contraction, suggesting that the cubic structure of the low-pressure phase could survive above 5.2 GPa. Three trigonal phases (*R3c*, no. 161) appeared in the pressure range of 9.7–50.7 GPa. Particularly, the cubic and trigonal-I phases coexisted around 7.2 GPa. The peak around 13.5° (marked by the star in Fig. 2a) gradually merged with the closed peak and disappeared under a pressure of 14.8 GPa, indicating that another phase (trigonal-II) transition occurred. Subsequently, the peaks in the range of 12–14° continued to merge into one peak when the pressure reached 26.5 GPa, revealing the trigonal-III phase emerging. Fig. 2b shows the typical Rietveld refinements of the XRD patterns at 1.0 GPa, 9.7 GPa, and 26.5 GPa. The refined structural information on trigonal Ag_3PO_4 matches well with that theoretically calculated, as shown in Tables S1–S4.† The good refinements confirmed that Ag_3PO_4 underwent phase transitions from cubic to trigonal structures under high pressure. To the best of our knowledge, this is the first observation of a pressure-induced phase transition from cubic to trigonal in the A_3XZ_4-type compounds.

The crystal structure refinement parameters of all diffraction patterns and the volume compressibility are summarized in Fig. 2c–e. Upon compression up to 50 GPa, the volume of Ag_3PO_4 shrinks by a quarter (Fig. 2e). Uncommonly, the *c*-axis of the trigonal-I and II (or Tri. I and Tri. II) phases exhibits

 This journal is © The Royal Society of Chemistry 2019

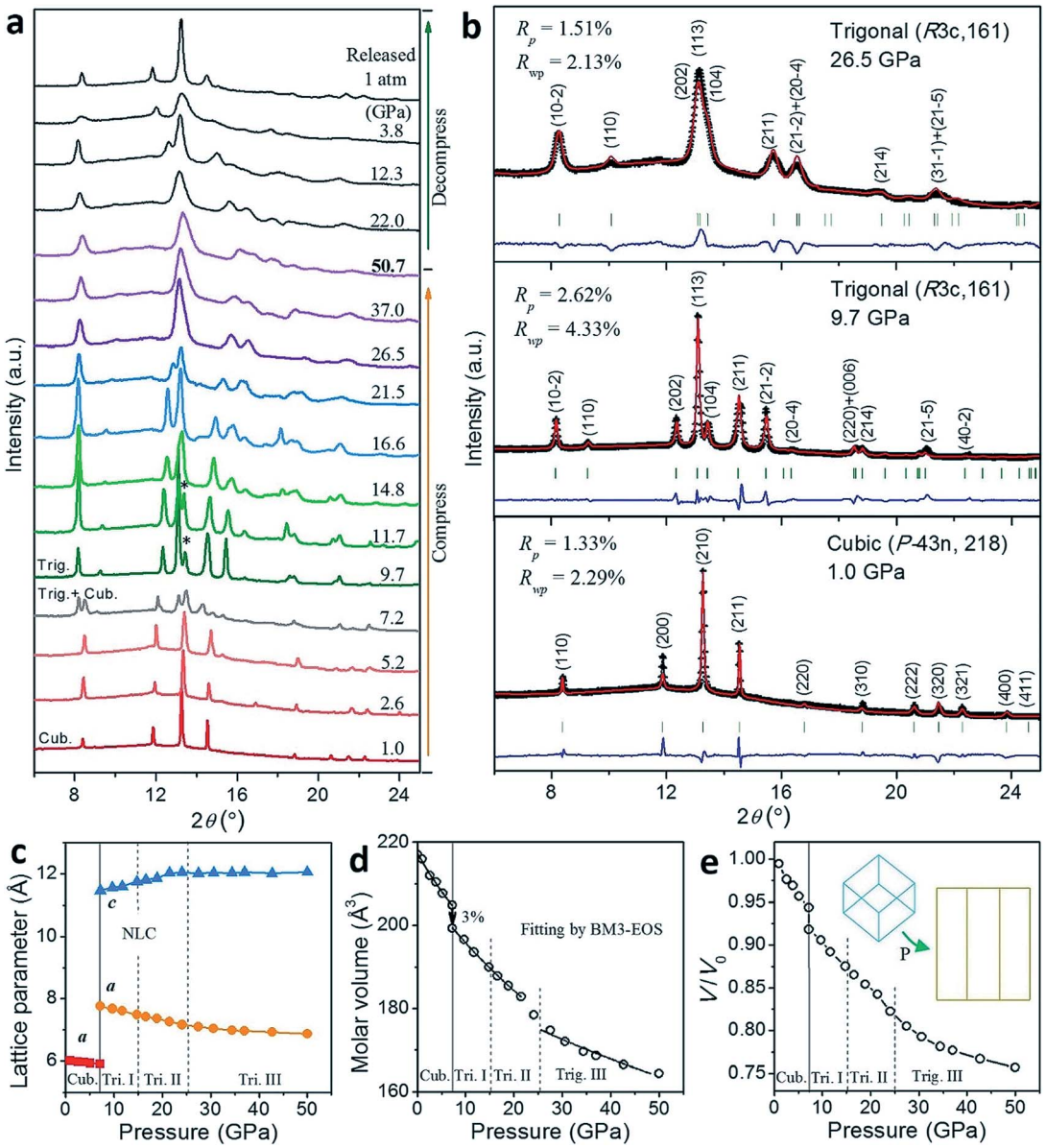

Fig. 2 (a) Synchrotron X-ray diffraction patterns of Ag_3PO_4 under both compression and decompression ($\lambda = 0.6199$ Å). (b) Rietveld refinements of the experimental (black fork) XRD data at 1.0 GPa, 9.7 GPa, and 26.5 GPa. The blue lines denote the difference between the experiments (black) and refinements (red), and the green vertical lines represent the refined peak positions. (c and d) Pressure-dependent lattice parameters and the molar volume of Ag_3PO_4. The relationship between the molar volume and pressure was fitted by the 3rd-order Birch–Murnaghan (BM3) equation of state (EOS) $P(V) = 3B_0 f_E(1+2f_E)^{5/2}\left[1+\frac{3}{2}(B_0'-4)f_E\right]$ where $f_E = [(V_0/V)^{2/3}-1]/2$ is the Eulerian strain, B_0 is the bulk modulus, B_0' is its pressure derivative, and V and V_0 are the unit cell volume and volume at zero pressure. (e) Variation of molar volume compressibility (V/V_0) as a function of pressure.

negative linear compressibility (NLC) with -3.02 to -2.87 TPa^{-1} (Fig. 2c). After the transition from the trigonal-II to trigonal-III phase around 26 GPa, the lattice parameter of c is steady, while a continues to decrease at a slower rate. Fig. 2d shows the volume–pressure relationship, with around a 3% percentage decrease of the molar volumes from the cubic to the trigonal-I phase around 7.5 GPa. In addition, a 3rd-order Birch–Murnaghan (BM3) equation of state (EOS) was employed to fit the experimental data belonging to each structure. Then, the EOS parameters were determined to have a bulk modulus of $B_0 =$ 101.29 GPa and a volume of $V_0 = 217.47$ Å^3 for the cubic Ag_3PO_4, $B_0 = 121.04$ GPa and $V_0 = 210.77$ Å^3 for the trigonal I and II structures, and $B_0 = 228.96$ GPa and $V_0 = 191.80$ Å^3 for the trigonal-III structure (Table 1). For cubic Ag_3PO_4, the bulk modulus is smaller than that in other ternary phosphates, suggesting that Ag_3PO_4 is soft like some metals and the ductile semiconductor α-Ag_2S with a bulk modulus of 59.7 GPa.[2,49,50] Therefore, the semiconducting Ag_3PO_4 could be applied to flexible devices, such as resistive random access memory.

After decompression to ambient pressure, the cubic structure of Ag_3PO_4 was recovered with hysteresis viewed from the shifted Bragg peaks, which agrees with the Raman observation.

Table 1 The EOS parameters for the different structures of Ag_3PO_4 determined from present experiments

Phase	B_0 (GPa)	B_0'	V_0 (Å^3)
Cubic	101.29	5.64	217.47
Trigonal-I, II	121.04	3.16	210.77
Trigonal-III	228.96	4.00 (fix)	191.80

This means that the pressure-induced phase transition of Ag_3PO_4 is partially reversible. Comparatively, the quenched sample possesses the same lattice parameter of 6.01 Å as the pristine sample, but with broadened peaks (Fig. S6†). Considering the rapid recovery of the [PO_4] tetrahedra from the high- to low-pressure phase (see Raman results), the hysteresis and broadening should be attributed to the slow movement of the silver atoms to their original positions in the cubic unit cell, which is related to the band gap hysteresis during compression.

To better understand the phase transition, structural predictions of Ag_3PO_4 were conducted using the Stochastic Surface Walking (SSW) method.[30,36,38] The pathway sampling was carried out initially using the VASP package starting from cubic Ag_3PO_4 (2 Ag_3PO_4 units per cell) to generate a database of pathways that connect Ag_3PO_4 with the other phases. In total, 120 pathways were collected from 500 SSW-crystal steps of pathway sampling. While the majority of the pathways (80) were found to convert from cubic Ag_3PO_4 to the trigonal-I phase, other pathways leading to phases such as monoclinic were also identified. The first principles DFT calculations based on the variable-cell double-ended surface walking method[30] were then utilized to verify the energetics of every low-energy pathway, from which the lowest energy reaction pathway was identified. The cubic phase to the trigonal-I phase is a one-step transition. The reaction profile is shown in Fig. 3a, starting from a cubic Ag_3PO_4 lattice to a trigonal-I phase lattice. We found that the phase transition is much simpler and only the [PO_4] polyhedra rotated. To our surprise, the phase transition barrier from the cubic phase to the trigonal-I phase is almost zero calculated by the NEB method at 7.5 GPa. This was indeed observed in our XRD experiments, where the phase transition takes place at 7.5 GPa. Furthermore, the simulated XRD patterns, volume-pressure relationship, and energy-volume relationship agree with the experimental results (Fig. S7 and S8†).

The phase transition of the Ag_3PO_4 from the cubic to trigonal phases is schematically shown in the insets of Fig. 3a, viewed from the $[111]_{Cubic}//[0001]_{Trigonal}$ orientation. Apparently, the applied pressure induced the change of the [AgO_4] polyhedra, then resulted in reversed rotation of around 10° for alternate [PO_4] tetrahedra along the $[111]_{Cubic}//[0001]_{Trigonal}$ direction. To obtain more details, the calculated bond lengths of the Ag–O, Ag–Ag, and P–O of Ag_3PO_4 under pressure are summarized in Fig. 3b–d. All the bond lengths split due to the rearrangement of atoms after the cubic–trigonal transition, revealing the symmetry destruction in the [AgO_x] polyhedron. As pressure increased, the bonds of the trigonal phase generally shrunk. Notably, one of the P–O bonds of the cubic and trigonal phases narrowed linearly with increasing pressure, which is reflected in

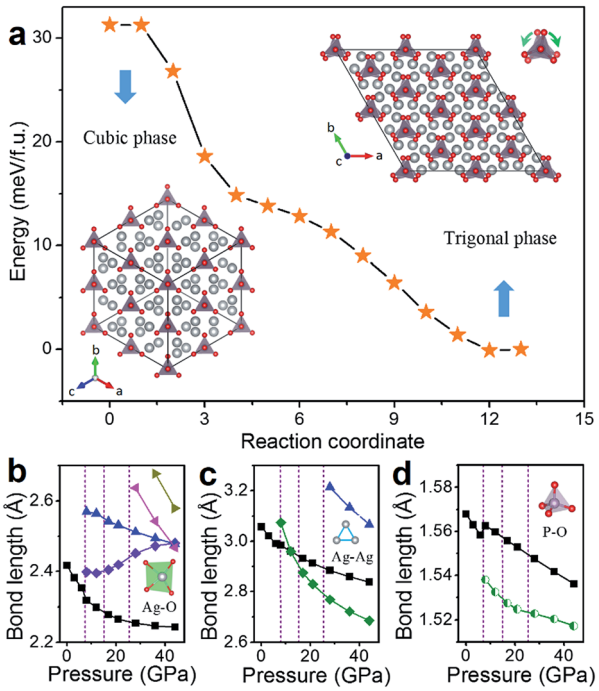

Fig. 3 (a) Calculated enthalpy of the phase transition at 7.5 GPa. Insets are the pressure-induced structural changes of the 2 × 2 × 2 unit cells viewed from the $[111]_{Cubic}//[0001]_{Trigonal}$ direction. (b–d) Theoretical bond lengths of Ag–O, Ag–Ag, and P–O as a function of pressure, respectively.

the Raman vibration (Fig. 3d and S5†). On the other hand, along the $[0001]_{Trigonal}$ direction, the regular [PO_4] tetrahedra were slightly squashed by 1–2%, and the [AgO_x] polyhedra underwent considerable distortion, resulting in the compact stacking of Ag_3PO_4 trigonal structures.

Discussion and conclusions

The optical properties and structural evolution of Ag_3PO_4, especially the [AgO_x] group change, are collated as follows: according to theoretical calculations, silver and oxygen atoms contribute mainly to the electronic structure and density of states (DOS) of Ag_3PO_4 (Fig. S9 and S10†). This is due to the fact that the top of the valence band and the bottom of the conduction band are dominated by Ag 5s and O 2p, like other silver compounds.[25,51] Here, the coordination number of Ag^+ and the scheme of the [AgO_x] group as a function of pressure were obtained and are shown in Fig. 4. The silver coordination of the trigonal-I phase is equal to that of the cubic phase, but alters the [AgO_4] structure and breaks its centrosymmetry. When pressure rises to 44 GPa, the silver coordination increases from 4 to 7, accompanying the dramatic coupling of neighboring atoms in the [AgO_x] configuration. On the other hand, the bond length of Ag–O in trigonal Ag_3PO_4 (Fig. 3b) decreases with increasing pressure. These trends lead to the band gap narrowing in trigonal Ag_3PO_4 upon compression.[52] Comparatively, the bond length of Ag–O in Ag_3PO_4 is still longer than that in the Ag_2O semiconductor (~2.0 Å at ambient). Hence, Ag_3PO_4

This journal is © The Royal Society of Chemistry 2019

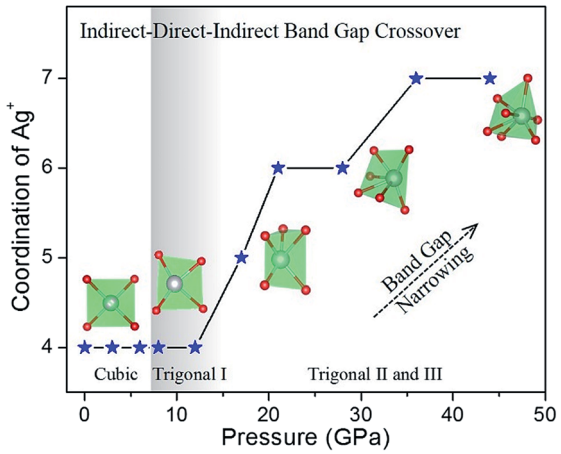

Fig. 4 Pressure-induced coordination change of silver in [AgO_x] polyhedra.

exhibits a wider band gap than Ag_2O. Furthermore, phosphorus atoms play a role in changing the configuration of the [AgO_x] matrix and prolonging the bond length, and in turn altering the electronic structure. For the quenched sample, the partial retainability of the band gap implies the distortion of the [AgO_x] polyhedra.

The indirect-to-direct band gap crossover usually occurs in transition metal dichalcogenides from bulk to a few layers especially to a monolayer, such as MoS_2, which originated from the quantum confinement effect.[53–56] Besides, the applied tensile strain and temperature rise can also effectively drive the band gap crossover, from indirect to direct *via* the common effect of crystal lattice expansion.[57,58] In contrast, pressure generally results in the shrinking of the crystal cell and the coupling of neighboring atoms, then a direct-to-indirect band gap transition, such as in CdSe and $CsPbBr_3$, under pressure.[59,60] In our case, prolonged partial Ag–O, Ag–Ag, and P–O bonds owing to the bond length splitting (Fig. 3b–d) may primarily degenerate the indirect and direct band gap in Ag_3PO_4 after the cubic-to-trigonal phase transition. The transitions between the indirect and direct band gap for Ag_3PO_4 display a good correlation with the Ag^+ coordination number and [AgO_x] configuration.

In conclusion, the pressure modulations in the optical properties and crystal structure of the malleable Ag_3PO_4 semiconductor were systematically studied by *in situ* synchrotron X-ray diffraction and optical absorption spectroscopy combined with theoretical calculations. Under compression, the band gap of Ag_3PO_4 was narrowed from ~2.4 eV to 1.8 eV *via* compression and the shrinking band gap could be partially retained after releasing the pressure to ambient pressure. In addition, the indirect-to-direct band gap crossover was discovered during the phase transition from the cubic to trigonal structure, as predicted by theoretical calculations. The pressure-driven band gap optimization and the indirect-direct band gap transitions are strongly correlated with the [AgO_x] configuration, including the bond length and the Ag^+ coordination number. These results may provide clues for understanding the underlying mechanism that causes the tuning of the electronic band structure and offer an opportunity to design better optoelectronic materials.

Author contributions

Y. L. conceived the idea, conducted the experiments, and wrote the manuscript. S.-C. Z. theoretically calculated the phase transition and optical properties. E. H. and G. L helped with manuscript revision. Y. H. helped with theoretical prediction of the high-pressure phase. J.-J. R. helped with XRD experiments. H. Y. supervised the work. All authors contributed to the manuscript revision and discussion.

Conflicts of interest

The authors declare no conflict of interest.

Acknowledgements

This work was financially supported by the National Natural Science Foundation of China (NSFC) (Grant Nos. U1530402 and 21703004). We are grateful to the Shanghai Synchrotron Radiation Facility (SSRF), Advanced Light Source (ALS), and Stanford Synchrotron Radiation Lightsource (SSRL) for use of their facilities. We also acknowledge Prof. Y. J. Lee of Yonsei University and HPSTAR for sharing synchrotron beam-time, Prof. L. Wang of HPSTAR for using his UV-VIS spectrometer, Prof. J. F. Shu of HPSTAR for his help with the high-pressure experiments, and Freyja O'Toole of HPSTAR for editing this manuscript.

References

1 Z. Yi, J. Ye, N. Kikugawa, T. Kako, S. Ouyang, H. Stuart-Williams, H. Yang, J. Cao, W. Luo, Z. Li, Y. Liu and R. L. Withers, *Nat. Mater.*, 2010, **9**, 559–564.
2 X. Shi, H. Chen, F. Hao, R. Liu, T. Wang, P. Qiu, U. Burkhardt, Y. Grin and L. Chen, *Nat. Mater.*, 2018, **17**, 421–426.
3 N. Lu, P. Zhang, Q. Zhang, R. Qiao, Q. He, H. B. Li, Y. Wang, J. Guo, D. Zhang, Z. Duan, Z. Li, M. Wang, S. Yang, M. Yan, E. Arenholz, S. Zhou, W. Yang, L. Gu, C. W. Nan, J. Wu, Y. Tokura and P. Yu, *Nature*, 2017, **546**, 124–128.
4 G. Y. Kim, A. Senocrate, T. Y. Yang, G. Gregori, M. Gratzel and J. Maier, *Nat. Mater.*, 2018, **17**, 445–449.
5 R. A. Kerner and B. P. Rand, *J. Phys. Chem. Lett.*, 2018, **9**, 132–137.
6 B. E. Mellander, *Phys. Rev. B*, 1982, **26**, 5886–5896.
7 H. Li, Y. Zhou, W. Tu, J. Ye and Z. Zou, *Adv. Funct. Mater.*, 2015, **25**, 998–1013.
8 S. Kim, Y. Wang, M. Zhu, M. Fujitsuka and T. Majima, *Chem.–Eur. J.*, 2018, **24**, 14928–14932.
9 M. S. Hsieh, H. J. Su, P. L. Hsieh, Y. W. Chiang and M. H. Huang, *ACS Appl. Mater. Interfaces*, 2017, **9**, 39086–39093.

10 Y. Fan, W. Ma, D. Han, S. Gan, X. Dong and L. Niu, *Adv. Mater.*, 2015, **27**, 3767–3773.
11 Z. Jiao, Y. Zhang, H. Yu, G. Lu, J. Ye and Y. Bi, *Chem. Commun.*, 2013, **49**, 636–638.
12 N. Umezawa, O. Shuxin and J. Ye, *Phys. Rev. B*, 2011, **83**, 035202.
13 Y. Bi, S. Ouyang, N. Umezawa, J. Cao and J. Ye, *J. Am. Chem. Soc.*, 2011, **133**, 6490–6492.
14 Y.-z. Ma, F. Cheng, W.-s. Liu, J. Wang and Y.-k. Wang, *Trans. Nonferrous Met. Soc. China*, 2015, **25**, 112–121.
15 O. Khaselev, *Science*, 1998, **280**, 425–427.
16 J. R. Bolton, S. J. Strickler and J. S. Connolly, *Nature*, 1985, **316**, 495–500.
17 Z. Chen, T. F. Jaramillo, T. G. Deutsch, A. Kleiman-Shwarsctein, A. J. Forman, N. Gaillard, R. Garland, K. Takanabe, C. Heske, M. Sunkara, E. W. McFarland, K. Domen, E. L. Miller, J. A. Turner and H. N. Dinh, *J. Mater. Res.*, 2011, **25**, 3–16.
18 B. D. James, G. N. Baum, J. Perez and K. N. Baum, U.S. Department of Energy, December 2009, final report.
19 X. Guan and L. Guo, *ACS Catal.*, 2014, **4**, 3020–3026.
20 F. Chen, Q. Yang, X. Li, G. Zeng, D. Wang, C. Niu, J. Zhao, H. An, T. Xie and Y. Deng, *Appl. Catal., B*, 2017, **200**, 330–342.
21 S. Zhang, S. Zhang and L. Song, *Appl. Catal., B*, 2014, **152–153**, 129–139.
22 W. Cao, Z. Gui, L. Chen, X. Zhu and Z. Qi, *Appl. Catal., B*, 2017, **200**, 681–689.
23 A. B. Trench, T. R. Machado, A. F. Gouveia, M. Assis, L. G. da Trindade, C. Santos, A. Perrin, C. Perrin, M. Oliva, J. Andrés and E. Longo, *Appl. Catal., B*, 2018, **238**, 198–211.
24 M. S. A. Hussien and I. S. Yahia, *J. Photochem. Photobiol., A*, 2018, **356**, 587–594.
25 G. Botelho, J. C. Sczancoski, J. Andres, L. Gracia and E. Longo, *J. Phys. Chem. C*, 2015, **119**, 6293–6306.
26 H.-K. Mao, X.-J. Chen, Y. Ding, B. Li and L. Wang, *Rev. Mod. Phys.*, 2018, **90**, 015007.
27 L. Kong, G. Liu, J. Gong, Q. Hu, R. D. Schaller, P. Dera, D. Zhang, Z. Liu, W. Yang and K. Zhu, *Proc. Natl. Acad. Sci. U. S. A.*, 2016, **113**, 8910–8915.
28 H. K. Mao, J. Xu and P. M. Bell, *J. Geophys. Res.: Solid Earth*, 1986, **91**, 4673–4676.
29 S. Klotz, J. C. Chervin, P. Munsch and G. Le Marchand, *J. Phys. D: Appl. Phys.*, 2009, **42**, 075413.
30 A. P. Hammersley, S. O. Svensson, M. Hanfland, A. N. Fitch and D. Hausermann, *High Pressure Res.*, 1996, **14**, 235–248.
31 V. D. R. Larson AC, *Los Alamos National Laboratory Report LAUR*, The Regents of the University of California, Los Alamos, NM, 1994, pp. 86–748.
32 B. H. Toby, *J. Appl. Crystallogr.*, 2001, **34**, 210–213.
33 D. Errandonea, C. Popescu, A. B. Garg, P. Botella, D. Martinez-García, J. Pellicer-Porres, P. Rodríguez-Hernández, A. Muñoz, V. Cuenca-Gotor and J. A. Sans, *Phys. Rev. B*, 2016, **93**, 035204.
34 X. J. Zhang, C. Shang and Z. P. Liu, *J. Chem. Theory Comput.*, 2013, **9**, 3252–3260.
35 C. Shang and Z. P. Liu, *J. Chem. Theory Comput.*, 2013, **9**, 1838–1845.
36 C. Shang and Z. P. Liu, *J. Chem. Theory Comput.*, 2012, **8**, 2215–2222.
37 C. Shang, X. J. Zhang and Z. P. Liu, *Phys. Chem. Chem. Phys.*, 2014, **16**, 17845–17856.
38 X.-J. Zhang, C. Shang and Z.-P. Liu, *J. Chem. Theory Comput.*, 2013, **9**, 5745–5753.
39 D. Sheppard, P. Xiao, W. Chemelewski, D. D. Johnson and G. Henkelman, *J. Chem. Phys.*, 2012, **136**, 074103.
40 G. Kresse and J. Furthmuller, *Phys. Rev. B*, 1996, **54**, 11169–11186.
41 J. Tauc, *Mater. Res. Bull.*, 1968, **3**, 37–46.
42 R. W. G. Wyckoff, *Am. J. Sci.*, 1925, **10**, 107–118.
43 L. Helmholz, *J. Chem. Phys.*, 1936, **4**, 316–322.
44 H. N. Ng, C. Calvo and R. Faggiani, *Acta Crystallogr.*, 1978, **34**, 898–899.
45 M. A. Lopez-Bote and S. Montero, *J. Raman Spectrosc.*, 1980, **9**, 386–392.
46 J. F. Boily, *J. Phys. Chem. A*, 2002, **106**, 4718–4724.
47 P. Dong, Y. Wang, B. Cao, S. Xin, L. Guo, J. Zhang and F. Li, *Appl. Catal., B*, 2013, **132–133**, 45–53.
48 Z. Wang, L. Yin, M. Zhang, G. Zhou, H. Fei, H. Shi and H. Dai, *J. Mater. Sci.*, 2013, **49**, 1585–1593.
49 P. Wang, R. Zhao, L. Wu and M. Zhang, *RSC Adv.*, 2017, **7**, 35105–35110.
50 R. Lacomba-Perales, D. Errandonea, Y. Meng and M. Bettinelli, *Phys. Rev. B*, 2010, **81**, 064113.
51 D. Santamaría-Pérez, E. Bandiello, D. Errandonea, J. Ruiz-Fuertes, O. Gomis, J. A. Sans, F. J. Manjón, P. Rodríguez-Hernández and A. Muñoz, *J. Phys. Chem. C*, 2013, **117**, 12239–12248.
52 G. Liu, L. Kong, J. Gong, W. Yang, H.-k. Mao, Q. Hu, Z. Liu, R. D. Schaller, D. Zhang and T. Xu, *Adv. Funct. Mater.*, 2017, **27**, 1604208.
53 A. Kuc, N. Zibouche and T. Heine, *Phys. Rev. B*, 2011, **83**, 245213.
54 K. F. Mak, C. Lee, J. Hone, J. Shan and T. F. Heinz, *Phys. Rev. Lett.*, 2010, **105**, 136805.
55 A. Splendiani, L. Sun, Y. Zhang, T. Li, J. Kim, C. Y. Chim, G. Galli and F. Wang, *Nano Lett.*, 2010, **10**, 1271–1275.
56 Y. Zhang, T. R. Chang, B. Zhou, Y. T. Cui, H. Yan, Z. Liu, F. Schmitt, J. Lee, R. Moore, Y. Chen, H. Lin, H. T. Jeng, S. K. Mo, Z. Hussain, A. Bansil and Z. X. Shen, *Nat. Nanotechnol.*, 2014, **9**, 111–115.
57 W. S. Yun, S. W. Han, S. C. Hong, I. G. Kim and J. D. Lee, *Phys. Rev. B*, 2012, **85**, 033305.
58 S. Tongay, J. Zhou, C. Ataca, K. Lo, T. S. Matthews, J. Li, J. C. Grossman and J. Wu, *Nano Lett.*, 2012, **12**, 5576–5580.
59 S. H. Tolbert, A. B. Herhold, C. S. Johnson and A. P. Alivisatos, *Phys. Rev. Lett.*, 1994, **73**, 3266–3269.
60 G. Xiao, Y. Cao, G. Qi, L. Wang, C. Liu, Z. Ma, X. Yang, Y. Sui, W. Zheng and B. Zou, *J. Am. Chem. Soc.*, 2017, **139**, 10087–10094.

 This journal is © The Royal Society of Chemistry 2019

Electronic Supplementary Material (ESI) for Journal of Materials Chemistry A.
This journal is © The Royal Society of Chemistry 2019

Supplementary Information

Pressure-driven band gap engineering in ion-conducting semiconductor silver orthophosphate

Yang Lu,‡[a] Shengcai Zhu,‡[ab] Eugene Huang,[a] Yu He,[ac] Jiaji Ruan,[a] Gang Liu[a] and Hao Yan*[a]

[a] *Center for High Pressure Science & Technology Advanced Research, Shanghai 201203, China*

[b] *Department of Physics and Astronomy, High Pressure Science and Engineering Center, University of Nevada, Las Vegas, NV 89154, USA*

[c] *Key Laboratory of High-Temperature and High-Pressure Study of the Earth's Interior, Institute of Geochemistry, Chinese Academy of Sciences, Guiyang, Guizhou 550081, China*

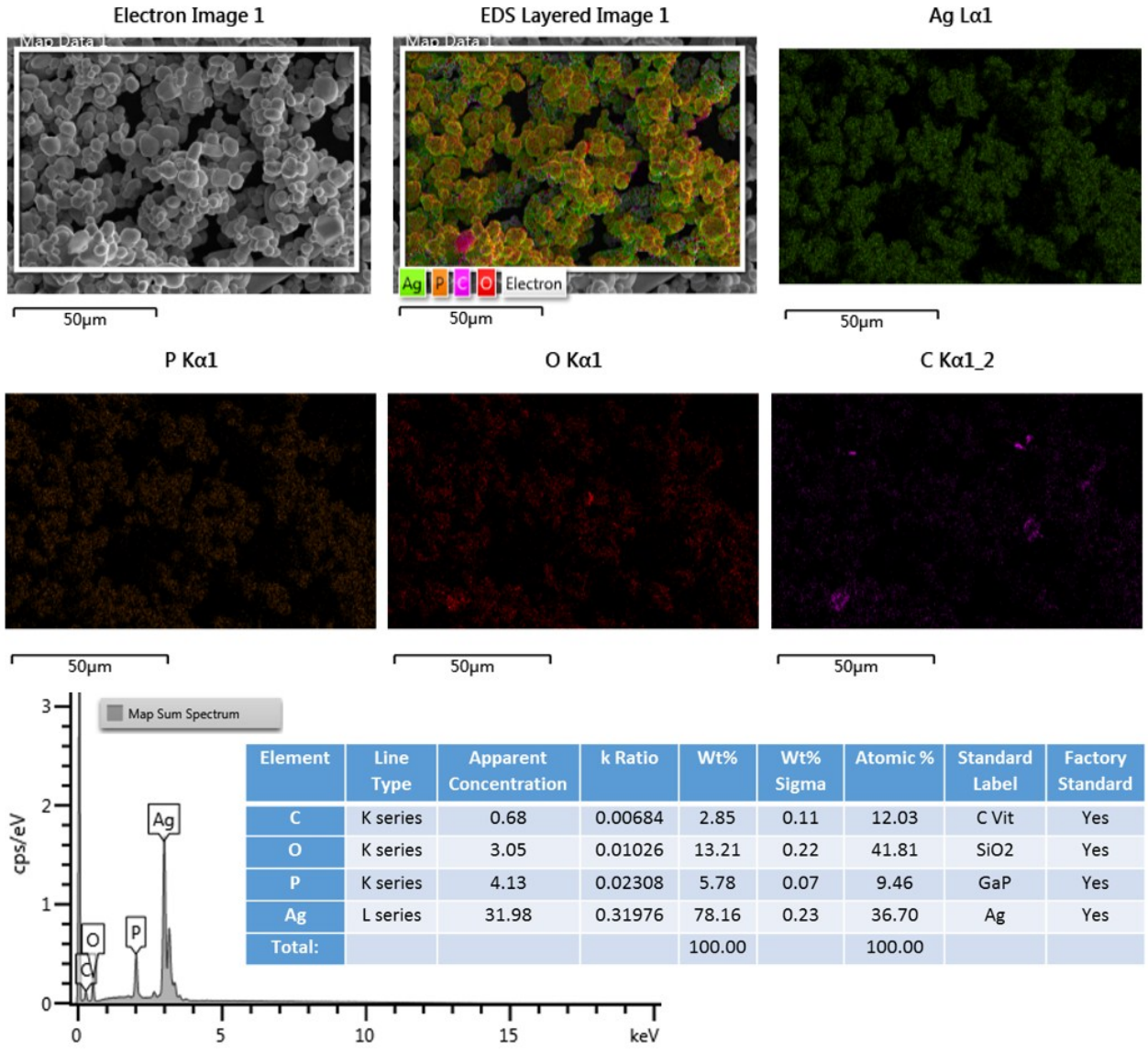

Element	Line Type	Apparent Concentration	k Ratio	Wt%	Wt% Sigma	Atomic %	Standard Label	Factory Standard
C	K series	0.68	0.00684	2.85	0.11	12.03	C Vit	Yes
O	K series	3.05	0.01026	13.21	0.22	41.81	SiO2	Yes
P	K series	4.13	0.02308	5.78	0.07	9.46	GaP	Yes
Ag	L series	31.98	0.31976	78.16	0.23	36.70	Ag	Yes
Total:				100.00		100.00		

Fig. S1 Elements analysis (EDX) of commercial Ag_3PO_4 powder before compression.

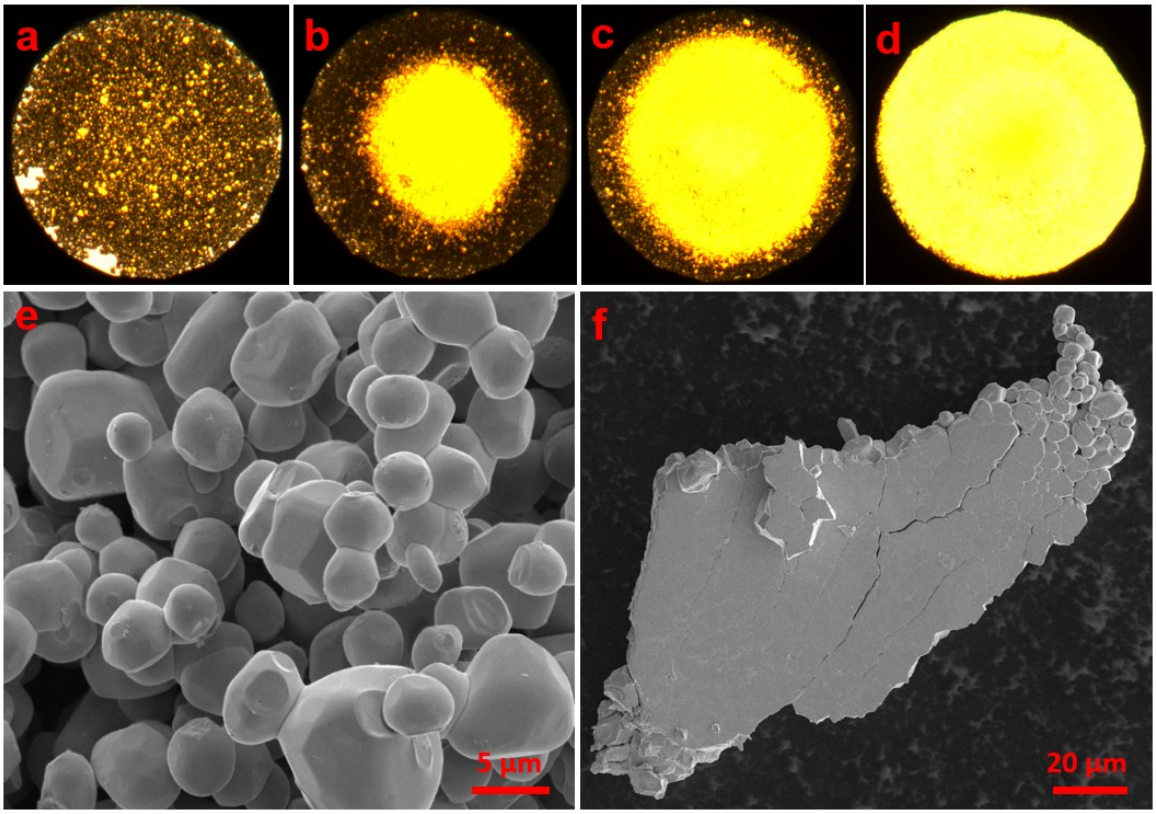

Fig. S2 (a-d) Photographs of the Ag_3PO_4 powder under increasing pressure by diamond anvil cell (500 μm of culets). (e and f) SEM images of the sample before and after compression.

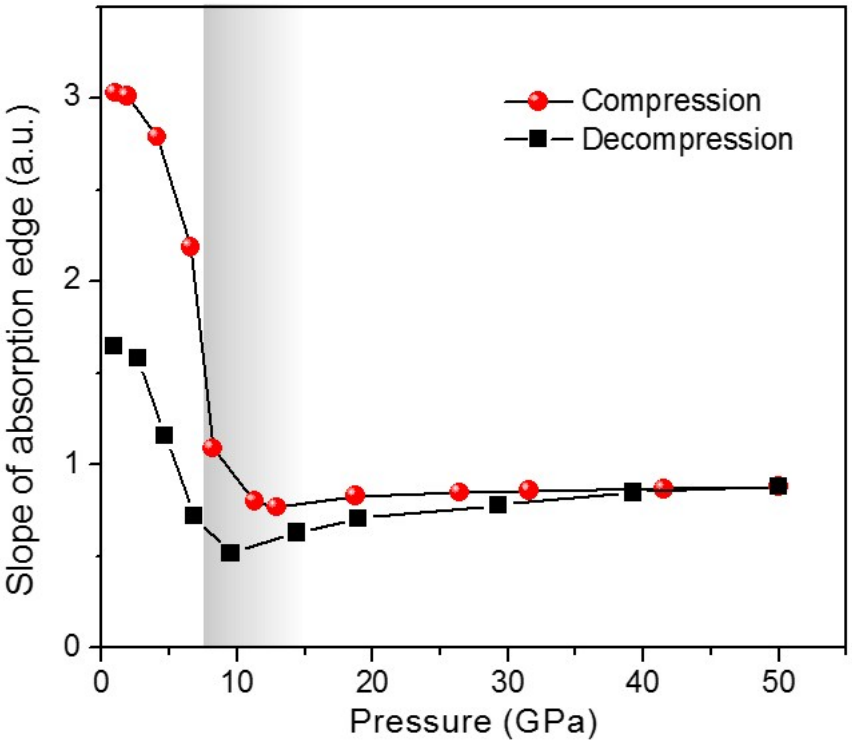

Fig. S3 Pressure-dependent slope of the absorption edge derived from the absorption spectra.

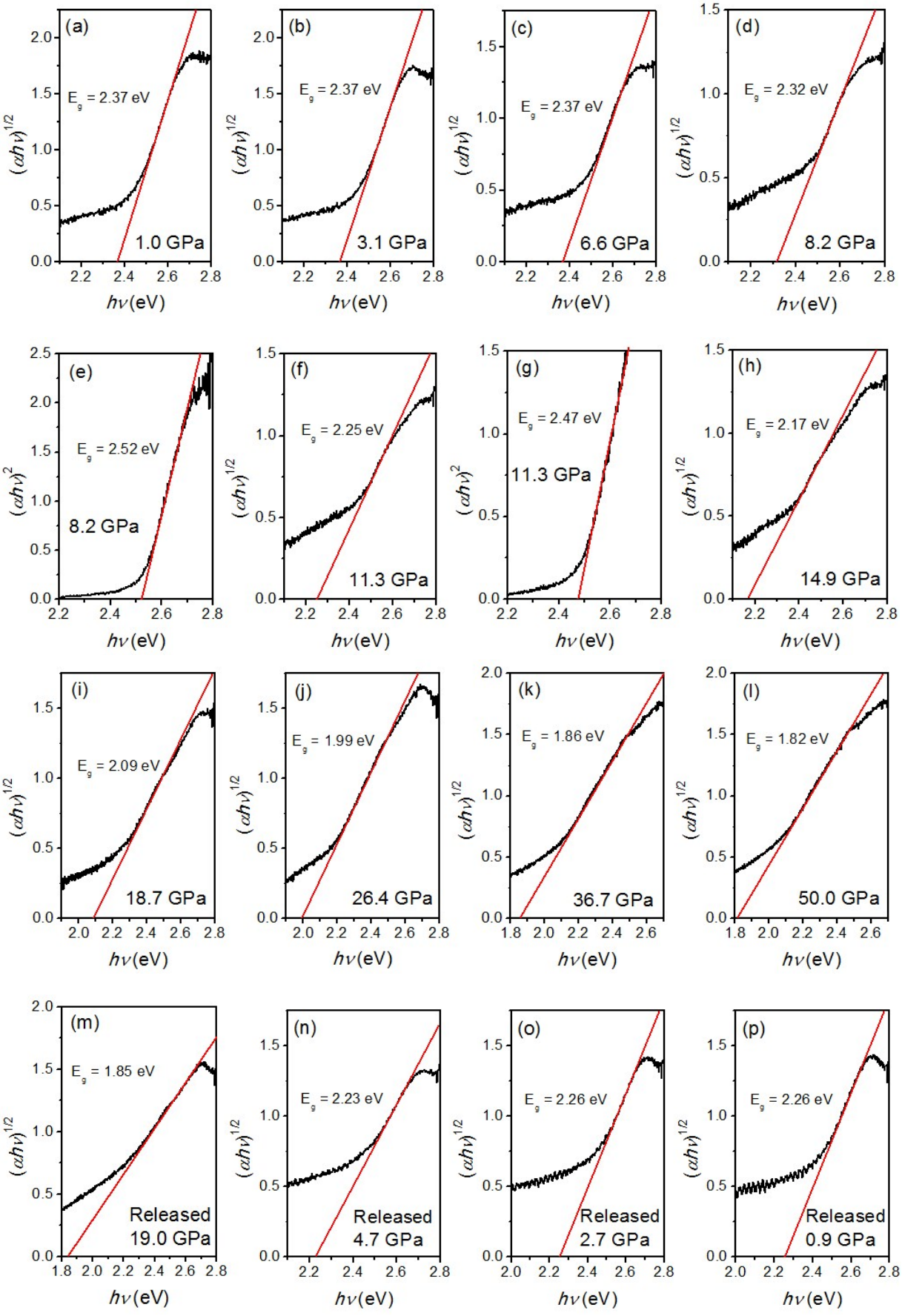

Fig. S4 Tauc plot of the absorbance data and the indirect/direct band gap value of Ag_3PO_4 under pressure.

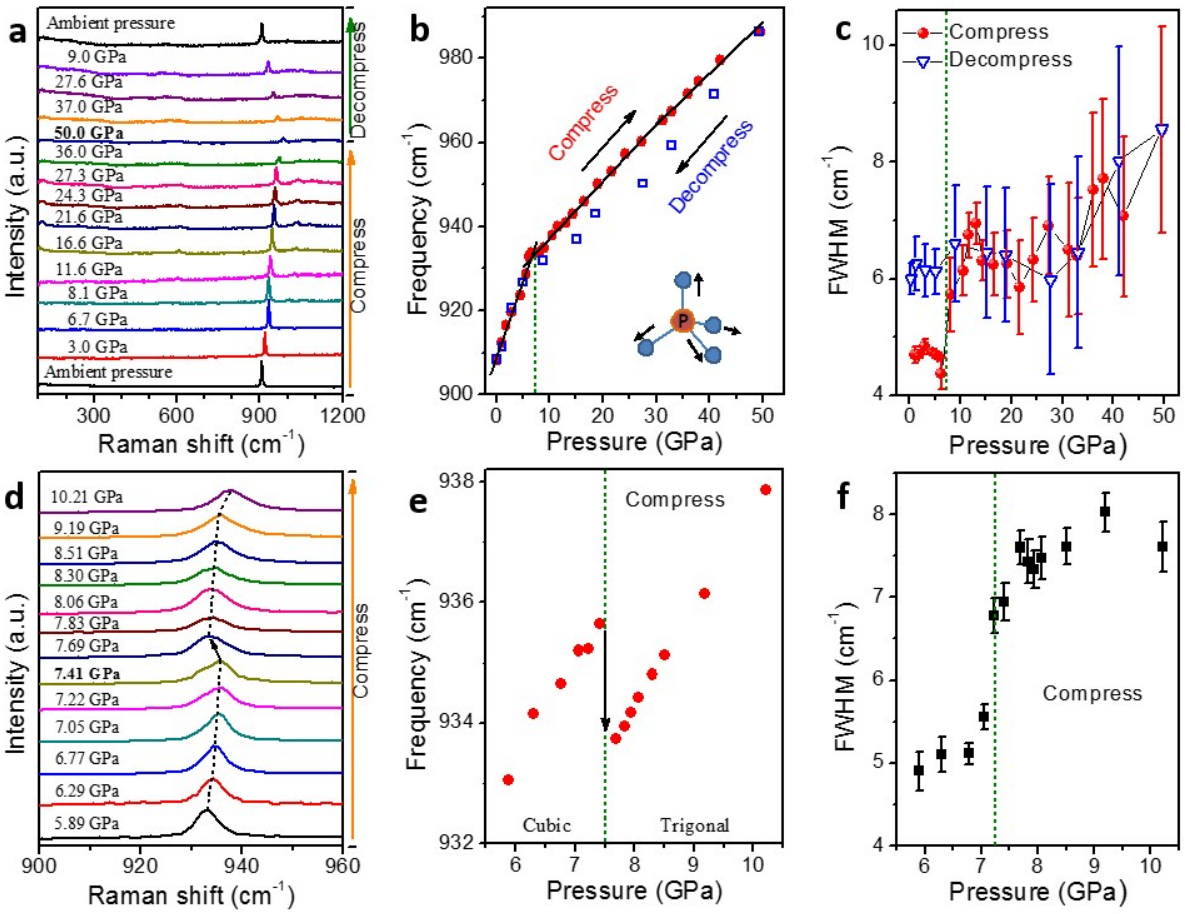

Fig. S5 (a) Selected Raman spectra of Ag_3PO_4 as a function of pressure at room temperature. (b) and (c) Pressure-dependent Raman shift and the full width at half maximum (FWHM) of the prominent peaks at Fig. S5(a), respectively. (d) Raman spectra of the Ag_3PO_4 sample under compression around the phase transition. (e) and (f) The pressure dependence of the frequency and FWHM of the Raman mode derived from Fig. S5(d), respectively.

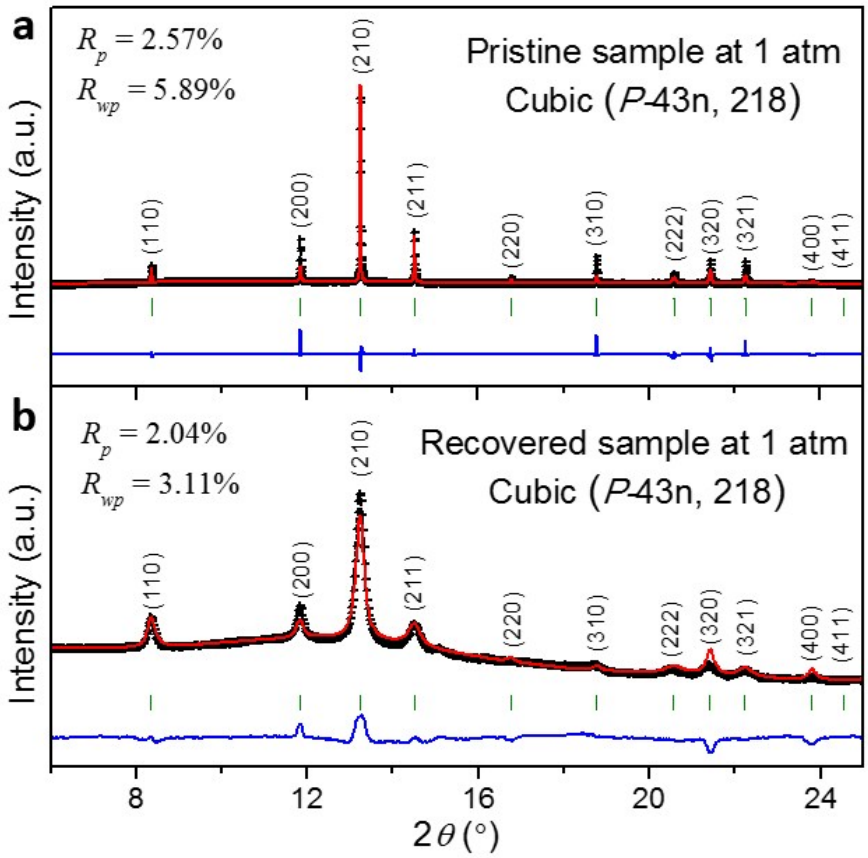

Fig. S6 Comparison between the synchrotron XRD spectra of the pristine sample (at 1 atm) and quenched sample after compression and decompression. (X-ray wavelength is 0.6199 Å)

Refined structural information of Ag_3PO_4 at 9.7 GPa

Table S1. Refined lattice data for Ag_3PO_4 at 9.7 GPa.

Title	Ag_3PO_4
Crystal system	Trigonal
Space group	*R*3c, 161
$a = b$ (Å)	7.67490
c (Å)	11.56120
$\alpha = \beta$	90°
γ	120°
V (Å^3)	589.76502

Table S2. Refined atomic positions and anisotropic displacement parameters for Ag_3PO_4 at 9.7 GPa.

Atom	*x*	*y*	*z*	Wyckoff site	U (Å^2)
Ag	0.68788	0.10834	-0.40531	18b	0.260
O1	0.20838	0.10491	-0.05453	18b	0.035
P	0.66667	0.33333	0.32800	6a	0.192
O4	0.66667	0.33333	-0.56327	6a	0.014

Calculated structural information of Ag_3PO_4 at 10.0 GPa

Table S3. Predicted lattice data for Ag_3PO_4 at 10.0 GPa.

Title	Ag_3PO_4
Crystal system	Trigonal
Space group	*R*3c, 161
$a = b$ (Å)	7.65190
c (Å)	11.72010
$\alpha = \beta$	90°
γ	120°
V (Å^3)	594.29286

Table S4. Predicted atomic positions and anisotropic displacement parameters for Ag_3PO_4 at 10.0 GPa.

Atom	*x*	*y*	*z*	Wyckoff site	U (Å^2)
Ag	0.68447	0.11574	-0.40249	18b	0.013
O1	0.21663	0.06749	-0.05270	18b	0.013
P	0.66667	0.33333	0.32565	6a	0.013
O4	0.66667	0.33333	-0.54339	6a	0.013

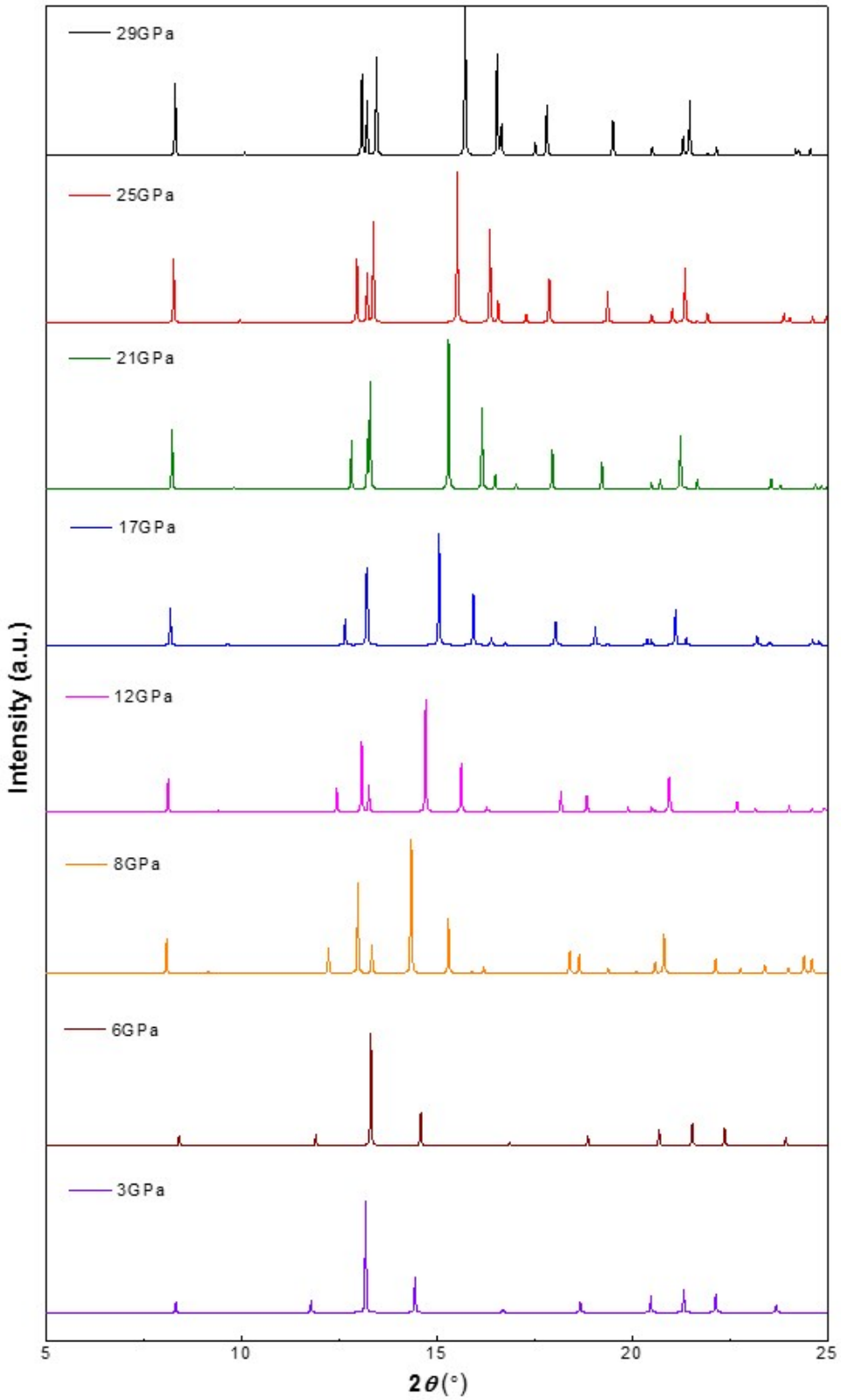

Fig. S7 Theoretical XRD patterns of Ag_3PO_4 under different pressure derived from the predicted crystal structures. (X-ray wavelength is 0.6199 Å)

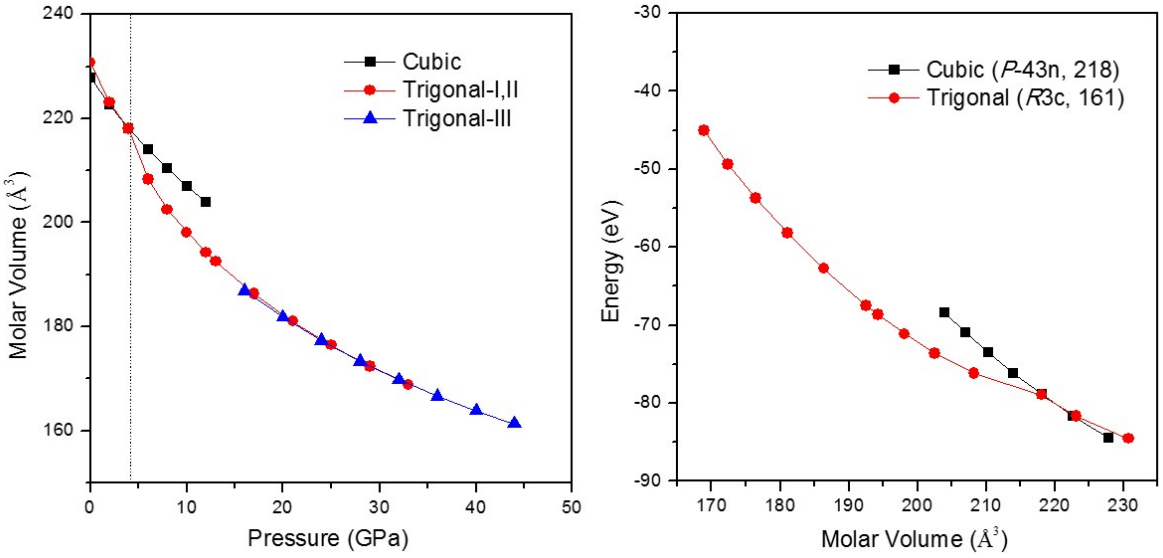

Fig. S8 Calculated volume-pressure plot (left) and energy-volume plot (right) of Ag_3PO_4.

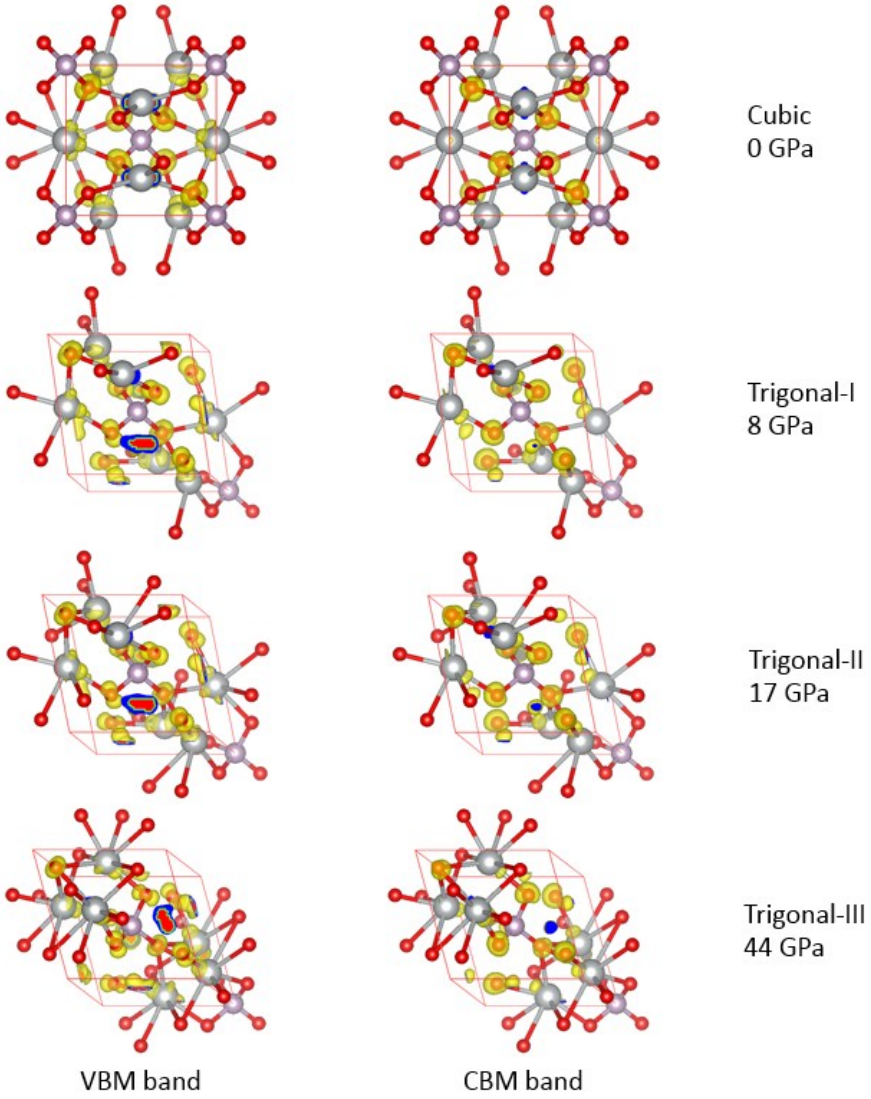

Fig. S9 Partial charge density of VBM and CBM bands for Ag_3PO_4. Grey spheres: Ag atoms; red spheres: O atoms; purple spheres: P atoms.

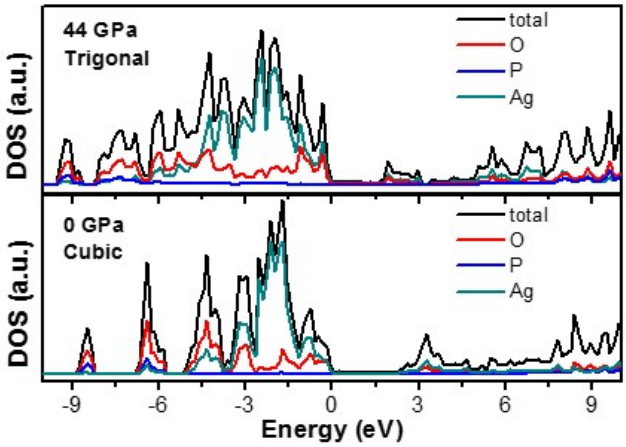

Fig. S10 Total and partial density of states (DOS) of the cubic (0 GPa) and trigonal (44 GPa) Ag_3PO_4.